This MICCAI paper is the Open Access version, provided by the MICCAI Society. It is identical to the accepted version, except for the format and this watermark; the final published version is available on SpringerLink.

OsteoOpt: A Bayesian Optimization Framework for Enhancing Bone Union Likelihood in Mandibular Reconstruction Surgery

Hamidreza Aftabi[1]*, John E. Lloyd[1], Amanda Ding[2], Benedikt Sagl[3],
Eitan Prisman[2], Antony Hodgson[4], and Sidney Fels[1]

[1] Department of Electrical and Computer Engineering, University of British Columbia, Canada `aftabi@student.ubc.ca`
[2] Department of Surgery, University of British Columbia, Canada
[3] Center of Clinical Research, Medical University of Vienna, Austria
[4] Department of Mechanical Engineering, University of British Columbia, Canada

Abstract. Mandibular reconstruction is crucial after oral tumor resection, yet current methods rely on premorbid geometric approximations and struggle with achieving reliable donor-native bone union. We propose a Bayesian optimization framework that enhances predicted bone union likelihood and facilitates computer-aided intervention by systematically varying key surgical parameters—resection plane orientation, donor bone positioning, and graft length—across three mandibular regions. Reconstruction performance is evaluated using two cost functions, coupled with a sensitivity analysis on modeling parameters. We validated the model using longitudinal patient-specific data from 5-day and 1-year postoperative CT and MRI scans. Our results show that optimization significantly enhances the predicted likelihood of bone union, with a relative improvement of up to 329% compared to the standard surgical practice. Additionally, validation shows a Dice coefficient of up to 0.76 between union prediction and actual postoperative imaging data. This study suggests that modifying the standard surgical plan can significantly improve bone union, underscoring the need for advanced optimization frameworks in surgical planning. The open-source code is available on GitHub.

Keywords: Mandibular Reconstruction Surgery · Optimization · Computer-Assisted Intervention · Computational Modeling

1 Introduction

The incidence of oral cancer has risen significantly in recent years. The American Cancer Society estimates that about 59,660 new cases of oral cavity and oropharyngeal cancer will be diagnosed in the U.S. in 2025 [1]. Many cases involve the mandible, necessitating resection and reconstruction to restore the jaw's contour and function [2]. Autologous bone grafting, primarily using fibula

---

* Corresponding author

or scapula grafts, is the gold standard for mandibular reconstruction [3]. However, nonunion at the graft-host interface remains a major challenge [4,5], with rates reaching up to 37% [4]. Such complications can cause pain, functional impairment, and, in severe cases, necessitate revision surgery.

Several studies have assessed the likelihood of bone union in mandibular reconstruction using simulations based on established bone remodeling algorithm [6,7,8,9]. While clinically evaluated in specific scenarios such as denture fixation [9] or mandibular reconstruction [6,7,8], these studies have some limitations. Existing methods lack automated design optimization for predicting bone union—typically focusing on implants or plates [10] while neglecting bone graft structure. In contrast to hardware modifications, which may lead to complications such as fracture or exposure [11], adjusting bone shape offers greater surgical flexibility. These studies also use simplified biomechanical models of the temporomandibular joint (TMJ) [12], muscle [3], and bone-to-bone contact, relying on static rather than dynamic simulations.

Building on prior works [13,14], (i) We develop a Bayesian optimization framework that enhances predicted bone union by efficiently exploring key design parameters. Integrating medical imaging and dynamic simulation, our method supports next-generation computer-aided intervention for personalized surgical planning that optimizes functional parameters beyond conventional geometry replication [15]. The open-source code is available on GitHub. (ii) We optimize three key but less explored parameters—resection plane orientation, donor vertical offset, and donor bone length—evaluating them across three mandibular defect types with two optimization cost functions. Robustness is assessed through sensitivity analysis. We hypothesize that our automated optimization can significantly improve bone union likelihood. (iii) Finally, we validate the model by comparing its predictions with longitudinal patient-specific imaging data.

2 Methods and Materials

2.1 Workflow

Our workflow (Fig.1) comprises three automated steps—Virtual Planning, Mesh Refinement, and Physics-based Simulation—integrated into the optimization process. The core implementation is in MATLAB, integrating external tools.

Virtual Planning: We used the ArtiSynth API [16] to reconstruct three defect cases based on Urken's Classification [17]. Using imaging data from [13], we generated three synthetic defects: body (B), symphysis (S), and ramus-body (RB). Surgeons define the resection plane positions based on defect type, while other angular and length-based variables are optimized through the program described in Sec. 2.2. The number and position of donor segments are determined using the Ramer-Douglas-Peucker (RDP) algorithm [18], which approximates the mandible's contour using straight-line segments. One segment is used to reconstruct B and S defects, while RB defects require two segments; however, the framework generalizes to any number of segments. RDP point offset controls the position of the intermediate cut between the two donor segments along

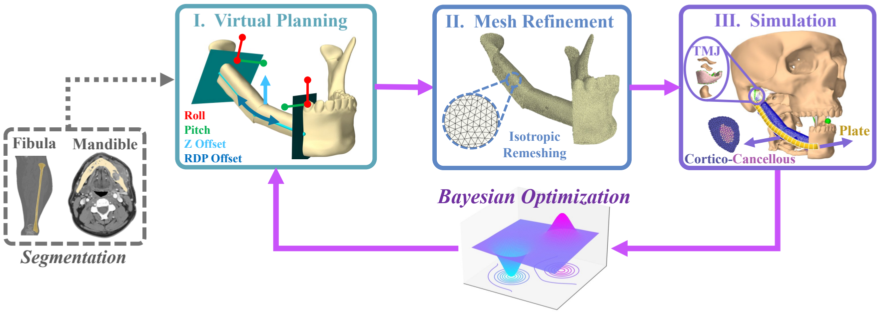

Fig. 1: The Bayesian optimization workflow includes virtual planning, mesh refinement, and simulation (RB baseline example with optimization parameters).

the mandible's curvature. To increase bony contact, a brute-force search is performed, analyzing overlapping planar polygons from resection and donor meshes to maximize apposition. Finally, a coarse finite element (FE) plate deforms to match the mandibular shape via axial springs in a forward simulation.

Mesh Refinement: We used PYMeshLab API [19] to refine the mesh before physics-based simulations. A mesh sensitivity analysis on maximum principal stress (MPS) determined the optimal edge length, stopping when changes fell below 5% to balance computational cost and accuracy. The process applies isotropic explicit remeshing to key anatomical structures with a target edge length of 0.50 mm, 50 refinement iterations. Additional steps merge close vertices, snap mismatched borders, remove duplicate faces, and repair non-manifold elements. Small holes are automatically closed using edge-based refinement to maintain structural integrity. The refined meshes are then used in physics-based simulations at each optimization iteration.

Physics-based Simulation: The reconstructed and refined meshes are reimported into ArtiSynth for physics-based biomechanical simulation. This study builds on the model from [13], which includes rigid bodies (resected mandible, maxilla, hyoid), 24 Hill-type muscles, ligaments, a food bolus with 110 N resistance, and a validated TMJ with FE capsule and rigid disc [12]. To model different defects, the corresponding muscles attached to each resection area were removed, as detailed in [13], which also provides information on muscle and ligament properties. We further extended the model by incorporating FE plate and a donor bone with cortical and cancellous layers. We used TetGen library [20] to generate a volumetric mesh from the refined surface mesh in the previous stage. We observed uniform cortical thickness and linearly mapped average Hounsfield unit (HU) to bone density (0.7–1.8 g/cm^3). Linear elastic material properties were set as $E = 13.7$ GPa, $\nu = 0.3$ for cortical bone and $E = 1.1$ GPa, $\nu = 0.3$ for cancellous bone [9]. To secure the donor segment in place, we incorporated a linear elastic titanium plate ($\rho = 4.42$ g/cm^3, $E = 100$ GPa, $\nu = 0.3$) with rigid locking screws at segment midpoints, connecting the nearest nodes of the plate and donor bone. The plate was attached to the resected mandible by di-

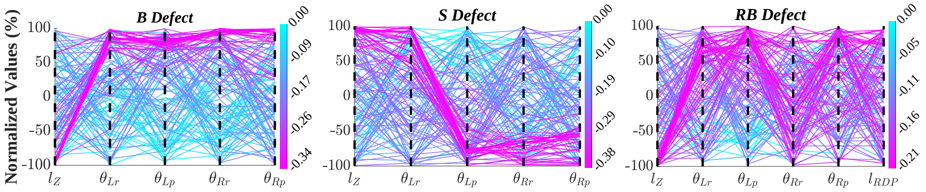

Fig. 2: Parallel chart of 150 iterations for three defects with F_{opt} objective. Parameters are normalized to $[-100, 100]$. Magenta marks the optimal region.

rectly linking its nodes to the mandible's surface. Our simulation models the contact between the mandible and donor bone using vertex penetration and the Aharonov–Jones–Landau (AJL) method [16]. To improve accuracy, we apply a linear elastic contact [21,13], with $E = 30$ KPa, $v = 0.3$, and a thickness of $t_{contact} = 0.2$ mm [10]. These parameters account for near-void soft tissue regions forming in early reconstruction and the typical gap at the interface [10]. To predict bone union, we used strain energy density (SED) normalized by apparent bone density, the primary mechanical stimulus for bone remodeling. Based on established remodeling algorithm [6,7,8,9,10], when the normalized SED, S, exceeds $S_0(1 + \S)$ with a lazy zone of $2\S = 0.2$ and $S_0 = 0.036$ mJ/g, bone growth occurs, enhancing bone apposition. At each time step, the normalized SED of each element is computed as $S = (1/2)(\sigma : \varepsilon)/\rho$, where σ and ε are the element stress and strain tensors, respectively, and ρ is the element apparent bone density. To assess remodeling, we overlaid a single element layer on each donor resection side and defined the apposition fraction as the ratio of elements exceeding the threshold to the total elements in the layer. We ran the ArtiSynth forward dynamics simulation of chewing with the non-reconstructed side and muscle activation set to pre-reconstruction levels to represent the early stage of reconstruction [13]. The simulation used a constrained backward Euler integrator (0.001s step) on a PC (16GB RAM, RTX 3060, i7-10700F@2.9GHz), averaging 6 minutes per iteration.

2.2 Optimization Framework

Parameters Setup: Optimization parameters include the angular variables for roll and pitch angles of the right and left resection planes, with $\theta_{Rp} = \theta_{Lp} = \theta_{Rr} = \theta_{Lr} = 0$, and two length parameters: the vertical donor offset (l_Z) and, for the two segment case, the RDP point offset (l_{RDP}), both initially set to zero (see Fig. 1). These baseline values are commonly used by surgeons. The parameters are grouped as follows:

$$\boldsymbol{\theta} = (\theta_{Lr}, \theta_{Lp}, \theta_{Rr}, \theta_{Rp})^T \in \mathbb{R}^4 \quad \text{(angular)}, \quad \boldsymbol{l} = (l_Z, l_{RDP})^T \in \mathbb{R}^2 \quad \text{(length)}. \tag{1}$$

The full parameter vector is $\boldsymbol{\phi} = (\boldsymbol{\theta}^T, \boldsymbol{l}^T)^T \in \mathbb{R}^6$, with the feasible region:

$$\mathcal{X} = \left\{\boldsymbol{\phi} \in \mathbb{R}^6 \mid \theta_{Lr}, \theta_{Lp} \in [-\alpha, \alpha], \theta_{Rr}, \theta_{Rp} \in [-\beta, \beta], l_Z \in [-z, z], l_{RDP} \in [-r, r]\right\}. \tag{2}$$

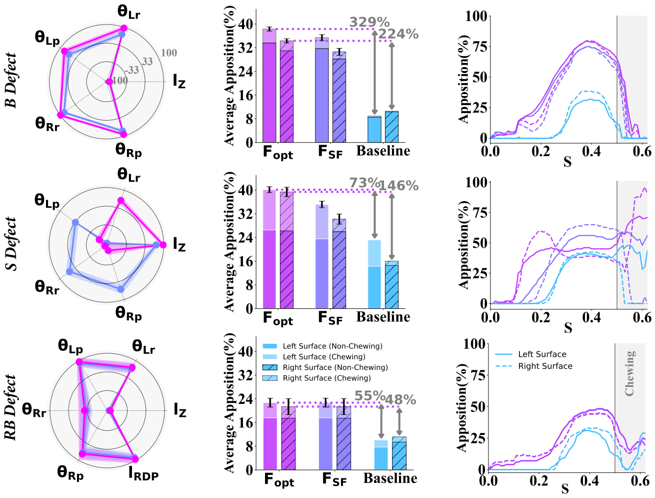

Fig. 3: Average of five trials showing mapped optimized parameters $[-100, 100]$ (col. 1), apposition average (col. 2), and apposition over time (col. 3) for three defects (rows) and objectives: F_{opt}, F_{SF}, and Baseline (parameters set to zero).

The parameter ranges for each defect type are chosen based on physical constraints, ensuring at most one tooth root is sacrificed and a 10–25 mm vertical gap between the fibula and maxillary teeth for implant placement [22]. The vector $(\alpha°, \beta°, z\,\text{mm}, r\,\text{mm})$ is set to $(25°, 20°, 3.5, -)$ for the B defect, $(15°, 15°, 5, -)$ for the S defect, and $(25°, 15°, 5, 7)$ for the RB defect. Jaw reconstruction effectiveness is assessed using apposition fractions over a chewing cycle with $n = 62$ data point (spanning 0.62 sec). Here, $L_i(\boldsymbol{\phi})$ and $R_i(\boldsymbol{\phi})$ denote the left and right fractions at each time step i, respectively, while $M_i(\boldsymbol{\phi})$ is defined as the minimum fraction from the contacting middle resection planes as they show similar behaviour. Their cycle averages are given by $\overline{X}(\boldsymbol{\phi}) = \frac{1}{n}\sum_{i=1}^{n} X$ for $X \in \{L, R, M\}$. We use $\overline{X}(\boldsymbol{\phi})$ in our cost functions, since sustained contact is key to union [23,2]. Two cost functions are then defined for optimization.

Cost Functions: The first cost function, F_{opt}, determines the optimal parameters by solving $\boldsymbol{\phi^*} = \arg\min_{\boldsymbol{\phi}} -(F_{opt})$ where

$$F_{opt} = W_1 \sum\nolimits_{X \in \{L,R,M\}} \overline{X}(\boldsymbol{\phi}) - W_2 \sum\nolimits_{X \neq Y \in \{L,R,M\}} |\overline{X}(\boldsymbol{\phi}) - \overline{Y}(\boldsymbol{\phi})|. \tag{3}$$

In this equation, the first term rewards high overall apposition by maximizing the sum of the average left, right, and middle apposition fractions, while the second term penalizes asymmetry between them. The coefficients $W_1 = W_2 = 0.5$ balance these contributions.

The second cost function, $F_{SF} = F_{opt} - \overline{C}$, builds upon the first by introducing a penalty term $\overline{C}$ for deviations in safety factor:

$$\overline{C} = \frac{1}{n} \sum\nolimits_{i=1}^{n} \sum\nolimits_{s \in \{\text{left,right}\}} w^s \left(\max(0, SF_{\text{desired}} - SF^s_{\text{worst},i})\right)^2. \tag{4}$$

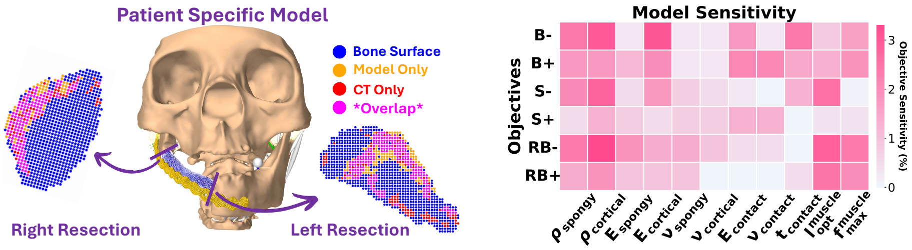

Fig. 4: Patient-specific validation against imaging data and sensitivity analysis.

The safety factor (SF) quantifies structural integrity, defined as the ratio of a bone's compressive yield strength to its maximum experienced stress, with $SF_{\text{desired}} = 1$. A higher SF indicates a lower failure risk. The worst-case safety factor for each side is computed as:

$$SF^{s}_{\text{worst},i} = \min\left\{ \frac{\sigma_{\text{yield, cortical}}}{\sigma^{s}_{\text{maxP, cortical},i}}, \frac{\sigma_{\text{yield, cancellous}}}{\sigma^{s}_{\text{maxP, cancellous},i}} \right\}, \quad s \in \{\text{left}, \text{right}\}. \quad (5)$$

Here, $\sigma^{s}_{\text{maxP, cortical/cancellous},i}$ represents MPS in each region on side s at time i during the chewing cycle. The yield stress values are set as $\sigma_{\text{yield, cortical}} = 100\,\text{MPa}$ and $\sigma_{\text{yield, cancellous}} = 5\,\text{MPa}$ [24].These parameters are selected to ensure optimization under worst-case scenarios, taking into account the region most prone to failure. The weighting factors $w^{s} = 0.5$ apply equal penalty contributions for both sides. These computationally expensive cost functions are then used within a Bayesian optimization.

Bayesian Optimization: To efficiently explore the parameter space $\boldsymbol{\phi} \in \mathbb{R}^6$ within the feasible region $\mathcal{X}$, we first generate $n_{\text{samples}} = 25$ points using a Sobol' sequence [25] (with a skip of 1000 and a leap of 100). Each sample is then linearly mapped to the feasible region by scaling the Sobol' values to the parameter limits. This initialization establishes quasi-uniform coverage of $\mathcal{X}$, reducing bias prior to Bayesian Optimization. The complete dataset at iteration N is defined by $\mathcal{D}_N = \{(\boldsymbol{\phi}_j, f_j)\}_{j=1}^{n_{\text{samples}}} \cup \{(\boldsymbol{\phi}_j, f_j)\}_{j=n_{\text{samples}}+1}^{N}$, where $f \in \{F_{opt}, F_{SF}\}$ and the first evaluations provide the initial sampling of $\mathcal{X}$. The subsequent evaluations are incorporated iteratively to refine the search. The computationally expensive function $f(\boldsymbol{\phi})$ is then modeled as a Gaussian Process (GP). Conditioned on the dataset $\mathcal{D}_N$, the posterior distribution of $f(\boldsymbol{\phi})$ is modeled as $f(\boldsymbol{\phi}) \mid \mathcal{D}_N \sim \mathcal{N}\Big(\mu_N(\boldsymbol{\phi}), \sigma_N^2(\boldsymbol{\phi}) + \sigma^2_{\text{noise}}\Big)$, where $\mu_N(\boldsymbol{\phi})$ denotes the posterior mean, $\sigma_N^2(\boldsymbol{\phi})$ the model-derived posterior variance, and σ^2_{noise} accounts for observation noise. To balance exploration and exploitation, the Expected Improvement Plus (EI+) acquisition function is used, prioritizing areas with the highest potential for improvement. The minimum observed function value among the dataset is defined as $\tilde{f}_{\text{min}} = \min\{f_j : (\boldsymbol{\phi}_j, f_j) \in \mathcal{D}_N\}$. with EI+ computation then follows [26]:

$$\mathrm{EI+}(\boldsymbol{\phi}) = \Big(\tilde{f}_{\min} - \mu_N(\boldsymbol{\phi})\Big)\Phi\left(\frac{\tilde{f}_{\min} - \mu_N(\boldsymbol{\phi})}{\sqrt{S(\boldsymbol{\phi})}}\right) + \sqrt{S(\boldsymbol{\phi})}\,\varphi\left(\frac{\tilde{f}_{\min} - \mu_N(\boldsymbol{\phi})}{\sqrt{S(\boldsymbol{\phi})}}\right). \tag{6}$$

where we define $S(\boldsymbol{\phi}) = \sigma_N^2(\boldsymbol{\phi}) + \sigma_{\text{noise}}^2$, and denote by $\Phi(\cdot)$ and $\varphi(\cdot)$ the cumulative distribution function and probability density function, respectively, of the standard normal distribution. The next sampling point is selected by solving $\boldsymbol{\phi}_{N+1} = \arg\max_{\boldsymbol{\phi}\in\mathcal{X}} \mathrm{EI+}(\boldsymbol{\phi})$.

2.3 Sensitivity Analysis & Validation

We analyzed model sensitivity by applying ±10% changes to 11 biomechanical parameters, including bone properties, elastic contact, and muscle parameters, and evaluated their impact on F_{opt} across all defect types. Each case was repeated five times, yielding a total of 330 simulations, with the average effect reported.

Moreover, beyond analyzing synthetic defect cases (B, S, and RB), we performed patient-specific validation using CT scans at 5 days and 1 year post-surgery, along with post-operative MRI. The patient, a 65-year-old female, underwent right ramus and body reconstruction with a scapular bone. The 5-day CT was used to segment the mandible, maxilla, hyoid, and plate in Slicer, capturing the early reconstruction stage. T1-weighted MRI was registered to CT using Elastix [27] for TMJ disc segmentation. TotalSegmentator [28] was used to segment four key masticatory muscles, and their physiological cross-sectional areas were determined using the method described in [6]. Muscle insertions and origins were manually assigned based on these segmentations, and the maximum lengths were obtained by scaling the resting lengths by a factor of 1.2 to 1.5 [13]. Several muscles/ligaments, similar to those excluded in the RB defect (except temporalis), were omitted. FE components for the donor bone, fixation plate, and TMJ capsule as well as simulation method followed Sec. 2.1. We used the method in 2.1 to estimate a uniform cortical thickness of 0.78 mm. Cortical and cancellous bone densities were set to $\rho = 1.45$ g/cm^3 and $\rho = 0.7$ g/cm^3, respectively, with other parameters unchanged. We assessed bone union likelihood over a full chewing cycle by tracking apposition fraction at the donor-mandible interface (resection sides). To assess prediction accuracy, the 1-year CT was segmented, and a 1-voxel-thick tensor quantified bone formation at the mandible-donor interface. Cortical bone percentage (*cort*%) was computed using an HU threshold of 1000 [29], a known marker of bone formation and successful union [30], generating a binary label map. We then used this percentage in the simulation to rank and select the top *cort*% of elements on the resection surface, prioritizing those that reached the apposition threshold and maintained contact for a longer duration over the chewing cycle [23,2], representing regions with prolonged bone-to-bone interaction. Finally, the centroids of these elements were interpolated using the Gaussian method to align with the imaging voxel grid, allowing direct correlation between simulation and clinical imaging data.

3 Results and Discussion

Fig. 3 illustrates the optimized parameters and the average apposition behavior over one chewing cycle for the three defect cases (B, S, and RB). The results show that peak apposition occurs during the mid-phase (lateral movement) and the end-phase (bolus chewing, gray background). The results, averaged over five simulations with random initial values and 50 iterations, demonstrate the robustness and efficiency of the optimization process, achieving optimal values with minimal observations. The optimization resulted in substantial relative improvements in predicted bone union— up to 329% for B, 146% for S, and 55% for RB—compared to the surgeon's common practice (baseline), while keeping the standard deviation low. Changing the cost function from F_{opt} to F_{SF} had minimal impact on B, no impact on RB, but altered the optimized values for S, which exhibited higher apposition during the bolus chewing phase, suggesting a more conservative optimization approach may be necessary to reduce failure risk. Moreover, the lower improvement in RB may result from extensive resection and significant muscle loss, reducing load at the mandible-donor interface. Additionally, to demonstrate the impact of each parameter on the cost function F_{opt}, we ran 150 iterations. Fig. 2 presents a parallel plot of the normalized variables and their effect on optimization. As this is a minimization problem, lower values indicate more favorable outcomes, shown in magenta. The results highlight the significant contribution of key surgical parameters, particularly for B and S defects, while for RB, the right resection parameter had less influence due to the lack of muscle and ligament support. While the Bayesian optimization was run sequentially, its parallelization capability could further reduce runtime for larger iterations. The sensitivity analysis further demonstrates the robustness of our modeling, as shown in Fig. 4. Varying the modeling parameters by ±10% resulted in less than a 4% change in the objective function.

Although the model we built upon had previously been validated against the literature for jaw movement, bite force, muscle activation, condyle motion, and bone remodeling [13,6,7,8,9], we further validated it using longitudinal patient-specific data. Because assigning different resection or donor positions within a single patient is not feasible, we assessed simulation accuracy by comparing the predicted bone likelihood with patient-specific observations. Fig. 4 illustrates the patient-specific model, with the right and left resection surfaces in blue. The simulation's predicted bone formation (orange), based on Sec 2.3, was compared to cortical bone formation observed in imaging (red). The overlap between prediction and imaging data (pink) yielded a Dice coefficient of 0.7 for the left surface and 0.76 for the right surface, indicating a strong correlation. However, some discrepancies may stem from missing patient-specific data, such as jaw movement, and modeling simplifications, particularly in screw modeling near the resections.

4 Conclusion and Future Directions

This study introduces an automated Bayesian optimization framework for key surgical variables, achieving up to a 329% improvement in predicted bone union.

While model predictions have been validated against patient-specific clinical data, larger datasets are needed for broader confirmation. To date, the approach has been tested in a single patient because obtaining longitudinal imaging at 5 days and 1 year post-surgery is challenging and not part of routine care; additional CT scans also raise radiation-exposure concerns, particularly for patients receiving adjuvant therapy.

Future work will refine the model by incorporating volumetric muscle representations and patient-specific data on mandibular kinematics, muscle activation, and bite force. We will also evaluate additional variables, such as screw positioning, and conduct usability testing with surgeons. Although outcome variability has not yet been fully studied across different patients, we hypothesize that individuals with similar defect types—classified according to Urken—will exhibit comparable responses; this will be investigated in future studies.

Acknowledgments. We gratefully acknowledge funding from the Terry Fox Research Institute and extend our sincere thanks to the ISTAR Group at the University of British Columbia for their invaluable support.

Disclosure of Interests. The authors have no competing interests to declare.

References

1. American Cancer Society. Oral cavity and oropharyngeal cancer: Key statistics. `https://www.cancer.org/cancer/types/oral-cavity-and-oropharyngeal-cancer/about/key-statistics.html`, 2025. Accessed: 2025-02-18.
2. Batchu Pavan Kumar, V Venkatesh, KA Jeevan Kumar, B Yashwanth Yadav, and S Ram Mohan. Mandibular reconstruction: overview. *Journal of maxillofacial and oral surgery*, 15:425–441, 2016.
3. Hamidreza Aftabi, Katrina Zaraska, Atabak Eghbal, Sophie McGregor, Eitan Prisman, Antony Hodgson, and Sidney Fels. Computational models and their applications in biomechanical analysis of mandibular reconstruction surgery. *Computers in Biology and Medicine*, 169:107887, 2024.
4. Brian Swendseid, Ayan Kumar, Larissa Sweeny, Tingting Zhan, Richard A Goldman, Howard Krein, Ryan N Heffelfinger, Adam J Luginbuhl, and Joseph M Curry. Natural history and consequences of nonunion in mandibular and maxillary free flaps. *Otolaryngology–Head and Neck Surgery*, 163(5):956–962, 2020.
5. Farahna Sabiq, Abhiram Cherukupalli, Mohammad Khalil, Linh K Tran, Jamie JY Kwon, Thomas Milner, James S Durham, and Eitan Prisman. Evaluating the benefit of virtual surgical planning on bony union rates in head and neck reconstructive surgery. *Head & Neck*, 46(6):1322–1330, 2024.
6. Keke Zheng, Zhipeng Liao, Nobuhiro Yoda, Jianguang Fang, Junning Chen, Zhongpu Zhang, Jingxiao Zhong, Christopher Peck, Keiichi Sasaki, Michael V Swain, et al. Investigation on masticatory muscular functionality following oral reconstruction–an inverse identification approach. *Journal of biomechanics*, 90:1–8, 2019.

7. Keke Zheng, Nobuhiro Yoda, Junning Chen, Zhipeng Liao, Jingxiao Zhong, Chi Wu, Boyang Wan, Shigeto Koyama, Keiichi Sasaki, Christopher Peck, et al. Bone remodeling following mandibular reconstruction using fibula free flap. *Journal of Biomechanics*, 133:110968, 2022.
8. Boyang Wan, Nobuhiro Yoda, Keke Zheng, Zhongpu Zhang, Chi Wu, Jonathan Clark, Keiichi Sasaki, Michael Swain, and Qing Li. On interaction between fatigue of reconstruction plate and time-dependent bone remodeling. *Journal of the Mechanical Behavior of Biomedical Materials*, 136:105483, 2022.
9. Clarice Field, Qing Li, Wei Li, Mark Thompson, and Michael Swain. Prediction of mandibular bone remodelling induced by fixed partial dentures. *Journal of biomechanics*, 43(9):1771–1779, 2010.
10. Ben M Ferguson, Ali Entezari, Jianguang Fang, and Qing Li. Optimal placement of fixation system for scaffold-based mandibular reconstruction. *Journal of the Mechanical Behavior of Biomedical Materials*, 126:104855, 2022.
11. Satoshi Onoda, Yoshihiro Kimata, Kiyoshi Yamada, Narushi Sugiyama, Tomoo Onoda, Motoharu Eguchi, and Nobuyoshi Mizukawa. Prevention points for plate exposure in the mandibular reconstruction. *Journal of Cranio-Maxillofacial Surgery*, 40(8):e310–e314, 2012.
12. Benedikt Sagl, Martina Schmid-Schwap, Eva Piehslinger, Michael Kundi, and Ian Stavness. A dynamic jaw model with a finite-element temporomandibular joint. *Frontiers in Physiology*, 10:1156, 2019.
13. Hamidreza Aftabi, Benedikt Sagl, John E Lloyd, Eitan Prisman, Antony Hodgson, and Sidney Fels. To what extent can mastication functionality be restored following mandibular reconstruction surgery? a computer modeling approach. *Computer Methods and Programs in Biomedicine*, 250:108174, 2024.
14. Hamidreza Aftabi, John E Lloyd, Benedikt Sagl, Amanda Ding, Eitan Prisman, Antony Hodgson, and Sidney Fels. Optimizing bone cuts enhances predicted bone union propensity in mandibular body reconstruction. In *2025 IEEE 22th international symposium on biomedical imaging (ISBI)*. IEEE, 2025.
15. Krishna Vyas, Waleed Gibreel, and Samir Mardini. Virtual surgical planning (vsp) in craniomaxillofacial reconstruction. *Facial Plastic Surgery Clinics*, 30(2):239–253, 2022.
16. John E Lloyd, Ian Stavness, and Sidney Fels. Artisynth: A fast interactive biomechanical modeling toolkit combining multibody and finite element simulation. *Soft tissue biomechanical modeling for computer assisted surgery*, pages 355–394, 2012.
17. Mark L Urken, Hubert Weinberg, Carlin Vickery, Daniel Buchbinder, William Lawson, and Hugh F Biller. Oromandibular reconstruction using microvascular composite free flaps: report of 71 cases and a new classification scheme for bony, soft-tissue, and neurologic defects. *Archives of Otolaryngology–Head & Neck Surgery*, 117(7):733–744, 1991.
18. Yotam Shkedy, Joel Howlett, Edward Wang, Jennifer Ongko, J Scott Durham, and Eitan Prisman. Predicting the number of fibular segments to reconstruct mandibular defects. *The Laryngoscope*, 130(11):E619–E624, 2020.
19. Alessandro Muntoni and Paolo Cignoni. PyMeshLab, January 2021.
20. Si Hang. Tetgen, a delaunay-based quality tetrahedral mesh generator. *ACM Trans. Math. Softw*, 41(2):11, 2015.
21. Yanhong Bei and Benjamin J Fregly. Multibody dynamic simulation of knee contact mechanics. *Medical engineering & physics*, 26(9):777–789, 2004.
22. Khanh Linh Tran, David H Yang, Edward Wang, Jennifer Inseon Ham, Angela Wong, Maharshi Panchal, Harkaran Singh Dial, James Scott Durham, and Eitan

Prisman. Dental implantability of mandibular reconstructions: Comparing free-hand surgery with virtual surgical planning. *Oral Oncology*, 140:106396, 2023.

23. Jitendra Prasad and Ajay Goyal. An invertible mathematical model of cortical bone's adaptation to mechanical loading. *Scientific reports*, 9(1):5890, 2019.
24. Elise F Morgan, Ginu U Unnikrisnan, and Amira I Hussein. Bone mechanical properties in healthy and diseased states. *Annual review of biomedical engineering*, 20(1):119–143, 2018.
25. Marissa Renardy, Louis R Joslyn, Jess A Millar, and Denise E Kirschner. To sobol or not to sobol? the effects of sampling schemes in systems biology applications. *Mathematical biosciences*, 337:108593, 2021.
26. Chao Qin, Diego Klabjan, and Daniel Russo. Improving the expected improvement algorithm. *Advances in Neural Information Processing Systems*, 30, 2017.
27. Stefan Klein, Marius Staring, Keelin Murphy, Max A Viergever, and Josien PW Pluim. Elastix: a toolbox for intensity-based medical image registration. *IEEE transactions on medical imaging*, 29(1):196–205, 2009.
28. Jakob Wasserthal, Hanns-Christian Breit, Manfred T Meyer, Maurice Pradella, Daniel Hinck, Alexander W Sauter, Tobias Heye, Daniel T Boll, Joshy Cyriac, Shan Yang, et al. Totalsegmentator: robust segmentation of 104 anatomic structures in ct images. *Radiology: Artificial Intelligence*, 5(5), 2023.
29. Mahadevappa Mahesh. The essential physics of medical imaging. *Medical physics*, 40(7):077301, 2013.
30. Michael Knitschke, Sophia Sonnabend, Fritz Christian Roller, Jörn Pons-Kühnemann, Daniel Schmermund, Sameh Attia, Philipp Streckbein, Hans-Peter Howaldt, and Sebastian Böttger. Osseous union after mandible reconstruction with fibula free flap using manually bent plates vs. patient-specific implants: a retrospective analysis of 89 patients. *Current Oncology*, 29(5):3375–3392, 2022.